Journal of Materials Chemistry A

ROYAL SOCIETY OF CHEMISTRY

COMMUNICATION

View Article Online
View Journal | View Issue

Cite this: J. Mater. Chem. A, 2025, 13, 918

Received 25th October 2024
Accepted 27th November 2024

DOI: 10.1039/d4ta07615j

rsc.li/materials-a

Effective sensing mechanisms of O_2 and CO on SnO_2 (110) surface: a DFT study†‡

Felipe Lipsky, *[a] Amanda F. Gouveia, [a] Fabrício R. Sensato,[b] Mónica Oliva, [a] Elson Longo, [c] Miguel A. San-Miguel [d] and Juan Andrés *[a]

The dissociative adsorption of O_2 on SnO_2 is pivotal for its gas-sensing performance, yet the underlying mechanisms remain open to debate and hamper widespread applications. In this study, we introduce a novel mechanism that advances the understanding of gas adsorption and activation on metal oxide semiconductor surfaces, coupling O_2 dissociation and CO oxidation in a unified process that redefines the Mars–van Krevelen mechanism. Detailed DFT simulations demonstrate that the electronic and structural properties of the SnO_2 (110) surface trigger the spontaneous stabilization of a neutral polaron upon oxygen vacancy formation, boosting the activation of O_2 and directly coupling its dissociation with CO oxidation, resulting in a highly energetically efficient process. Our findings mark a paradigm shift in the understanding of O_2-driven gas-sensing technology and showcases how the polaron reduces activation barriers and stabilizes key intermediates, optimizing the catalytic cycle and the sensor activity. This work paves the way for the development of high-performance SnO_2-based sensors by leveraging defect engineering and polaron dynamics.

1 Introduction

SnO_2, an n-type semiconductor with a broad band gap of 3.6 eV, is widely recognized for its application in detecting harmful gases in contemporary gas sensor technology.[1–4] Its non-toxic and cost-effective nature, combined with high electron mobility, chemical stability, and heat resistance, make SnO_2 highly sensitive to a variety of hazardous gases and the material of choice for numerous applications, particularly in environmental monitoring and safety devices.[5–10]

The structural and electronic properties of SnO_2 are profoundly influenced by intrinsic defects, especially oxygen vacancies (V_O), which are commonly formed during synthesis. These vacancies arise from the reduction of SnO_2 to SnO, leading to the formation of Sn^{2+} species. V_O can exist in various charge states: neutral (fully occupied by two electrons), singly positively charged (with one electron), or doubly positively charged (completely unoccupied by electrons).[11–13] These vacancies introduce donor levels that promote n-type semiconductor behavior by generating additional electrons, thus enhancing SnO_2's effectiveness in gas-sensing applications, especially because these defects extend SnO_2's light absorption from the ultraviolet into the visible or infrared spectrum.[14–16] Excess electrons located within lattice defects such as the V_O deform the highly polarizable crystal lattice and facilitate the formation of polarons, which consist of the electrons and an associated lattice deformation. The local displacement of ions from their equilibrium positions creates a potential well, wherein the coupled charge and lattice deformation jointly contribute to carrier transport, significantly affecting the material's conductivity and reactivity.[17,18] Large polarons form shallow defect states, allowing carriers to move more freely with higher mobility and longer lifetimes, whereas small polarons exhibit phonon-assisted hopping transport, which lowers carrier mobility and reduces their lifetime.

Although the behavior of bulk V_O is well understood, gas adsorption—a critical aspect of SnO_2-based gas sensing—is fundamentally a surface phenomenon. Surface V_O are vital in determining the chemi-resistive sensing performance, acting as active donor or acceptor sites that enhance interactions with adsorbate molecules, thus further improving SnO_2's effectiveness in gas sensing applications.[19] However, the atomistic mechanisms governing surface V_O behavior remain unclear, limiting the optimization of gas sensing performance.[20] Therefore, an in-depth investigation into the role of surface V_O in gas adsorption, charge transfer, and redox energetics is necessary to

[a]Universitat Jaume I, Castelló de la Plana, Castelló 12071, Spain. E-mail: lipsky@uji.es; andres@qfa.uji.es

[b]Universidade Federal de São Paulo, Diadema, São Paulo 09913-030, Brazil

[c]CDMF, Universidade Federal de São Carlos, São Carlos, São Paulo 13565-905, Brazil

[d]Universidade Estadual de Campinas, Campinas, São Paulo 13083-970, Brazil

† This work is dedicated to Prof. Dr Celso Aldao, who recently passed away. An excellent person and an innovative researcher in sensor materials. He opened the way for us to develop this investigation.

‡ Electronic supplementary information (ESI) available. See DOI: https://doi.org/10.1039/d4ta07615j

gain a more comprehensive understanding of the underlying physics and to advance SnO_2's efficacy in sensor technologies.

The interaction of O_2 with semiconductor surfaces is pivotal to a variety of surface processes, such as the oxidation of O_2 and carbon monoxide (CO) molecules. In metal oxide semiconductors, this interaction plays a decisive role in governing their chemiresistive gas sensing behavior, where the adsorption and activation of oxygen species critically influence the material's sensing capabilities.[21–26] The prevailing sensing mechanism is primarily governed by the oxygen ionosorption model,[27–33] where the adsorption and activation of O_2 depend on electron transfer from the conduction band (CB) to the O_2 molecule once the molecules diffuse toward the SnO_2 surface, resulting in the formation of chemisorbed negative oxygen species, such as O_2^-, O^-, or O^{2-}, depending on the operating temperature.[34–36] For n-type semiconductors like SnO_2, this electron withdrawal creates an electron depletion layer, whereas a hole accumulation layer is formed for p-type semiconductors. These layers directly influence the material's resistance, which either increases or decreases depending on the nature of the gas interaction.[37,38]

Upon exposure to target gases, its adsorbed molecules react with surface-bound activated oxygen species, either releasing the trapped electrons to the surface (in the case of reducing gases) or extracting additional electrons from it (for oxidizing gases). This interaction directly modulates the width of the electron depletion or hole accumulation layer, thereby altering the resistance of the metal oxide semiconductor and determining its gas sensor sensitivity. Ultimately, the basic sensing mechanism is related to redox reactions on the surface that cause electron transfer, leading to a change in resistance.[39,40]

In a landmark study, Sopiha *et al.*[41] investigated the stability of charged oxygen species on pristine SnO_2 surfaces, and identified the formation of O^{2-} and O^- through the capture of electrons from the CB. Crucially, they identified O^{2-} as the key species driving the chemiresistive sensing response of SnO_2. Furthermore, they demonstrated that the surface morphology drives the generation of Sn^{2+} cations, rather than the typical Sn^{4+}, which plays a pivotal role in stabilizing these oxygen species. Charged systems were utilized in their simulations to elucidate the effect of charged oxygen defects on the SnO_2 sensor mechanism.

CO is a toxic gas with severe environmental and health risks, requiring highly efficient detection methods.[42–44] On SnO_2 surfaces, CO sensing is intimately linked to the surface composition and the presence of V_O, which enhance interactions with atmospheric oxygen, forming electron-trapping, activated oxygen species. Upon CO adsorption, it is oxidized by O^- or O^{2-}, producing CO_2. This process releases the previously trapped electrons back into the CB of SnO_2, which modulates the material's conductivity and triggers the sensor's response.[45–48]

Recent studies have investigated the direct oxidation of CO by lattice oxygen on SnO_2 surfaces. Lu *et al.*[49] revealed that CO oxidation on the reduced SnO_{2-x} (110) surface proceeds *via* the Mars–van Krevelen mechanism, wherein lattice oxygen acts as oxidizing agent following O_2 adsorption and dissociation. However, this model neglects the inherent instability of reduced SnO_2 surfaces under the oxygen-rich conditions typical of atmospheric exposure.[50]

Despite significant advancements in the understanding of metal oxide semiconductor gas sensors, the mechanisms underlying CO detection on SnO_2 remain a topic of active debate. Both the ionosorption and direct lattice oxidation models hinge on the prior dissociation of the O_2 molecule—a process that demands substantial energy input—thereby fueling ongoing controversy regarding the precise nature of oxygen species and their role in gas sensing. Our findings shed light on these mechanisms and offer a foundation for guiding surface engineering strategies aimed at enhancing gas-sensing performance. By tailoring surface composition and electronic properties, interactions with target gases can be strengthened, enabling improved toxic gas capture with faster response and recovery times. This approach optimizes the availability and reactivity of surface sites, providing a pathway for developing sensors with superior sensitivity and selectivity.

In this work, we rigorously model and analyze the sensing mechanisms associated with V_O on the SnO_2 (110) surface through advanced theoretical simulations. Our approach tackles two critical challenges: first, we accurately characterize V_O, revealing its pivotal role in modulating the energetics of redox reactions central to CO sensing. Second, we demonstrate that the Mars–van Krevelen mechanism arises naturally, as the dissociation of chemisorbed O_2 occurs simultaneously with CO oxidation to CO_2, in an energetically favorable process. These findings reveal a synergistic interplay between V_O and electron polarons, which couples O_2 dissociation and CO oxidation. This interplay not only enhances our understanding of the structural and electronic factors governing SnO_2's gas-sensing properties but also provides crucial insights into the relationship between material defects and sensing performance, paving the way for the design of more efficient, high-performance sensors.

2 Results and discussion

We demonstrate that V_O on the SnO_2 (110) surface plays a crucial role in enhancing gas sensing performance. Our computational analysis reveals that V_O induces spontaneous polaron formation, which localizes charge, thereby promoting O_2 adsorption and activation. This, in turn, drives O_2 dissociation, directly coupling with CO oxidation in a novel variation of the Mars–van Krevelen mechanism. The result is a highly efficient reaction pathway that regenerates the system's polaron and significantly enhances surface reactivity. Detailed characterization of the transition states involved in this mechanism is provided in the ESI,‡ with the methodology of our first-principles calculations outlined in Section 4.

2.1 Crystal structure

SnO_2 crystallizes in the rutile structure with a tetragonal unit cell ($P4_2/mnm$ space group), where each Sn^{4+} cation is octahedrally coordinated to six O^{2-} anions (Sn_{6c}), and each O^{2-} anion is bonded to three Sn^{4+} cations in a trigonal planar configuration (O_{3c}). The unit cell contains two SnO_2 formula units (Fig. SM-1a‡). The calculated lattice parameters ($a = b = 4.748$

Å, c = 3.208 Å) are in excellent agreement with experimental data (Table SM-1‡).[51]

The calculated band gap energy (E_g) is 2.78 eV, corresponding to a direct Γ → Γ transition (Fig. SM-2‡). While slightly underestimated compared to experimental values,[52] this result significantly improves upon those obtained using the GGA functional (Table SM-1‡). Additionally, Mulliken charge analysis shows that O_{3c} ions carry a charge of $-1.05|e|$ and Sn_{6c} ions are charged $2.09|e|$, reflecting their nominal oxidation states of −2 and +4, respectively. These values serve as benchmarks for evaluating oxidation states in the surface models.

2.2 Surface models

The SnO_2 (110) surface was chosen for adsorption studies due to its stability among low-index surfaces.[49,53] A (2 × 2) periodic slab model, with an 18 Å vacuum in the z-direction, was used. This model consists of three symmetric O–Sn_2O_2–O trilayers, totaling 72 atoms. The bottom trilayer was fixed to simulate bulk effects, and a dipole correction was applied to eliminate spurious electrostatic interactions. The surface energy converged at 1.706 J m^{-2} (Fig. SM-3‡).

The surface's exposed layer contains two distinct sites: octahedral Sn_{6c} and distorted square pyramidal Sn_{5c} (Fig. 1). Mulliken charges for Sn_{6c} and Sn_{5c} were 2.05 and $2.10|e|$, respectively. O anions also adopt two configurations: trigonal planar O_{3c} and bent O_{2c}, with Mulliken charges of -1.01 and $-1.07|e|$, respectively. Thus, the charge distribution of surface cations and anions closely mirrors that of the bulk.

The V_O in the SnO_2 (110) surface was then modeled by selectively removing one oxygen atom from the pristine slab. Two symmetrically distinct configurations of V_O were considered: the trigonal planar O_{3c} and the bent O_{2c} sites. The relative stability of these vacancies, denoted as V_O^q where q is the charge state, was evaluated based on their respective Gibbs formation energies G_f:[54]

$$G_f(V_O^q) = G_t(V_O^q) - G_t(SnO_2) + \frac{1}{2}G_t(O_2) + \mu_O + q\varepsilon_F + \Delta^q \quad (1)$$

$G_t(V_O^q)$ represents the total energy of the supercell containing an V_O in charge state q, while $G_t(SnO_2)$ corresponds to the total energy of the pristine surface using the same supercell. The oxygen anion removed from the crystal is assumed to enter an oxygen reservoir, with its chemical potential referenced to half of the total energy of an isolated O_2 molecule, $G_t(O_2)$. The Fermi level, ε_F, is referenced to the valence band (VB) maximum. The term Δ^q serves as a correction, ensuring the proper alignment of the electrostatic potentials between the defect and pristine supercells, while also accounting for finite-size effects that influence the total energies of charged defects.

Oxygen's chemical potential μ_O is a variable that must satisfy the stability condition of SnO_2, namely: $\mu_{Sn} + 2\mu_O = \Delta H_f(SnO_2)$, where μ_{Sn} is the chemical potential of Sn (referenced to bulk Sn). In the extreme O-rich limit, $\mu_O = 0$. In the extreme O-poor limit, μ_O is bounded by the formation of SnO: $\mu_{Sn} + \mu_O < \Delta H_f$(SnO), and thus: $\mu_O = \Delta H_f(SnO_2) - \Delta H_f(SnO)$. The phase diagram of allowed values is depicted in Fig. SM-4.‡ The calculations for neutral charge states revealed that the vacancy is more favorable on bent O_{2c} anions (Table SM-2), and the resulting structure is depicted in Fig. 1c.

Upon comparison with the pristine system, the introduction of a V_O, resulting from the removal of an O_{2c} anion, leads to a pronounced localization of charge density at the V_O site (Fig. 2a). This behavior contrasts with the delocalized CB and VB edges observed in the pristine structure. The presence of the V_O defect reduces the nominal charge of the adjacent cations from Sn^{4+} to Sn^{2+}, as reflected in a Mulliken charge decrease from 2.10 to $1.87|e|$.

The formation of Sn^{2+} cations induces local lattice distortions (Fig. 2b), which stabilize the electron localization through electron-lattice coupling. The two nearest-neighbor Sn cations exhibit an outward relaxation, moving away from the V_O site to strengthen bonding with the surrounding lattice. This relaxation reduces the overlap between the Sn dangling bonds, shifting the V_O defect state to a higher energy. The stability of the Sn cation in this more reduced form accommodates the

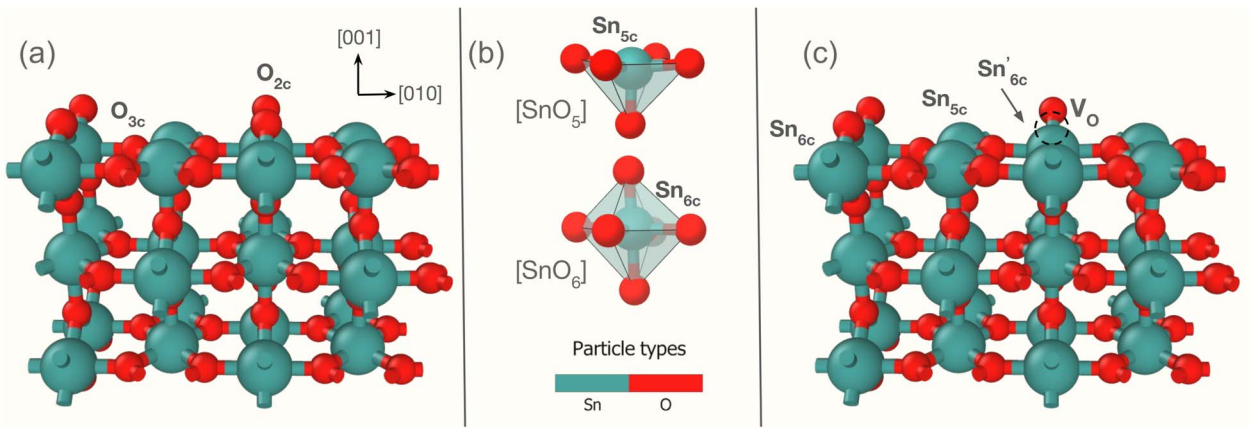

Fig. 1 (a) Structure of the pristine SnO_2 (110) surface, showing three O–Sn_2O_2–O trilayers. (b) Detailed view of the Sn clusters, with notation indicating the different coordination states of Sn ions used in this work. (c) Structure of the defective SnO_2 (110) surface featuring the most stable V_O. The prime symbol denotes the change in coordination of Sn cations brought about by the defect.

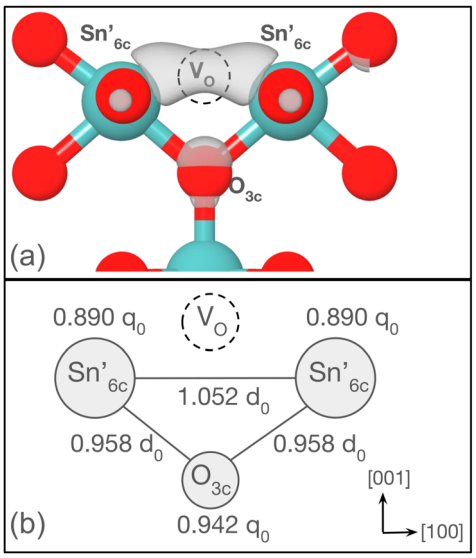

Fig. 2 (a) Charge density distribution of the A_1 state associated with the neutral V_O. The isosurface represents 10% of the maximum charge density. (b) Local structural relaxations around the V_O, showing deviations in bond distances (d_0) and charges (q_0) relative to the pristine structure.

localized excess charge effectively, facilitating polaron stabilization at the surface.

The introduction of a V_O generates a highly localized state approximately 0.33 eV below the conduction band minimum (CBM), which is occupied by two electrons (Fig. 3). This localized state resides well below the CB edge, effectively preventing thermal excitation and electron transfer to the CB. This electron localization and associated lattice rearrangement results in the formation of an electron polaron, confined between two neighboring Sn'_{6c} cations and constituted primarily of the 5s orbitals of these cations. This tight confinement and orbital occupation reflect the classic characteristics of a small electron polaron, where the electron's spatial localization and associated lattice distortion collectively stabilize the polaronic state.

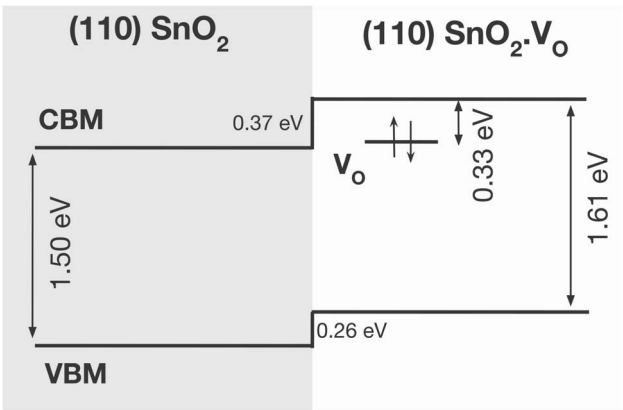

Fig. 3 Calculated position of the single-particle A_1 state of the neutral V_O in the SnO_2 (110) surface. The pristine and defect band structures are aligned to the vacuum potential. The composition of the band edges is discussed in the text.

By allowing the system to relax without any charge constraints, we identified this neutral oxygen vacancy as the most stable defect configuration. This aligns with Ágoston's seminal findings,[50] which indicate that singly charged vacancies are inherently unstable. Additionally, doubly charged vacancies would be ineffective in facilitating oxygen activation as it relies on electron availability.

The polaron state primarily arises from the adjacent Sn'_{6c} 5s orbitals, with a minor contribution from the O_{3c} 2pz orbital beneath the vacancy. The electronic structure can be qualitatively explained by molecular orbital theory. Removal of an O_{2c} atom, which is coordinated to two Sn_{6c} atoms and positioned above an O_{3c} site, creates two Sn dangling bonds with 5s character. These 5s orbitals (a_1 symmetry) combine into symmetric (A_1) and antisymmetric (B_2) orbitals. The A_1 orbital interacts with the O_{3c} 2pz orbital (b_1 symmetry), retaining predominantly A_1 character. This interaction reduces the point-group symmetry from D_{2h} (pristine) to C_{2v} around the vacancy.

Density of states (DOS) projections onto the top two trilayers show that the composition of the band edges is delocalized: the VB is mainly composed of O(2p) states with minor Sn(5p) and Sn(4d) contributions, while Sn(5s) states dominate the CB, with notable O(2p) contributions (Fig. SM-5‡). The CB's delocalized Sn(5s) states provide a low density of states near the CB edge, which combined with a sufficient wide band gap, favoring the polaron localization in the mid-gap region.

The creation of V_O raises both the VB maximum and CB minimum by 0.26 and 0.37 eV, respectively, widening the band gap. The formation of V_O, as discussed in the Introduction section, extends the light absorption range by introducing localized states within the band gap, shifting the initial absorption from the visible in the pristine surface to the infrared region in the defect system.

2.3 Oxygen ionosorption

Extensive screening of O_2 adsorption sites on the pristine SnO_2 (110) surface (Fig SM-6 and Table SM-3‡) reveals that O_2 predominantly interacts through physisorption atop Sn^{4+} cations in [SnO_{5c}] clusters, consistent with previous findings.[41] The most stable configuration involves triplet O_2 ($^3O_2$, $\mu = 2.00\mu_B$), which forms a weak dipole interaction with the surface ($\Delta_{ad}G = -0.23$ eV). Singlet O_2 ($^1O_2$, $\mu = 0.00\mu_B$) can also form at the same site by coordinating additionally with a neighboring bent O_{2c} anion, but it is energetically unfavorable ($\Delta_{ad}G = 0.21$ eV) and separated by a 0.16 eV energy barrier from the more stable triplet form (Fig. SM-7‡). Thus, singlet O_2 formation on the pristine surface is unlikely.

The electronic properties of adsorbed $^3O_2$ exhibit distinct features in the projected density of states (PDOS) (Fig. 4a) compared to $^1O_2$ (Fig. 4b). The triplet state shows two unoccupied peaks in the spin-down channel corresponding to its $2\pi^*$ antibonding orbitals, which are filled in the spin-up channel, reflecting a parallel spin configuration. Conversely, singlet O_2 has one unoccupied peak in the spin-up channel and one occupied peak in the spin-down channel, reflecting opposite spins in one $2\pi^*$ orbital.

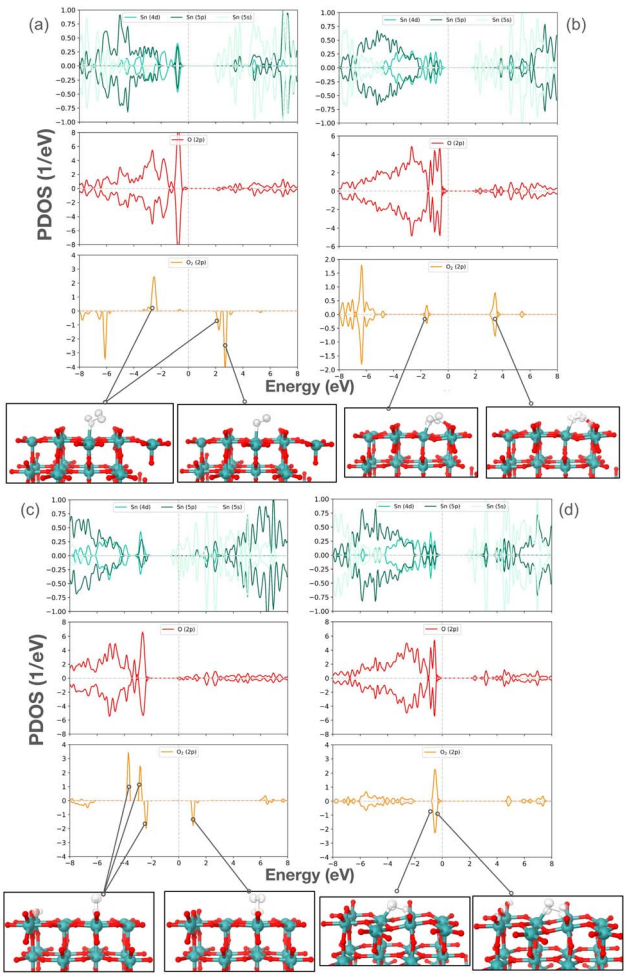

Fig. 4 Projected density of states (PDOS) for O_2 adsorbed on (a and b) pristine and (c and d) defective SnO_2 (110) surface. Insets depict charge densities projected on defect states, at 10% of maximum charge density. PDOS of the first surface trilayer (Sn: green, O: red) and the adsorbed molecule (orange) are shown, excluding population densities below 0.1 eV^{-1}. Band edges were aligned to the vacuum.

The O_2/SnO_2 interaction is weak, as indicated by minimal changes in the E_g and VB/CB edges upon adsorption, relative to the clean surface PDOS (Fig SM5a‡). This suggests that O_2 on the pristine SnO_2 (110) surface is unlikely to significantly influence sensor performance. The primary interaction arises from repulsion between the partially filled $2\pi^*$ orbitals of O_2 and the fully occupied VB maximum (VBM), where the VBM orbitals, primarily the 2p orbitals of bent O_{2c} atoms, lie too deep for stable hybridization, resulting in repulsion.

On the defective SnO_2 (110) surface, O_2 adsorption at the V_O site yields significantly different outcomes depending on the orientation of the adsorbed molecule. The defect site acts as a reduction center by utilizing trapped electrons in the shallow localized state created by the vacancy. The O_2 molecule can adsorb either vertically (Fig. 4c) or horizontally (Fig. 4d) over the vacancy, leading to the formation of a superoxide radical ($^{\bullet}O_2^-$, $\mu = 0.80\mu_B$) or a peroxide anion (O_2^{2-}, $\mu = 0.00\mu_B$), respectively. The adsorption energies are highly favorable, with $\Delta_{ad}G$ values of −1.10 eV for the superoxide radical and −1.99 eV for the peroxide anion. These stable chemisorption states arise from strong electrostatic interactions due to charge transfer from the surface to the adsorbate, unlike the weak dipole interactions observed on the defect-free surface.

The DOS analysis reveals that $^{\bullet}O_2^-$ formation is marked by a single unoccupied spin-down peak corresponding to one of the $2\pi^*$ antibonding orbitals (inset Fig. 4c), accompanied by the emergence of an occupied spin-down peak, absent in $^3O_2$. In contrast, O_2^{2-} formation is indicated by the full occupation of both $2\pi^*$ antibonding orbitals, as evidenced by occupied states in both spin-up and spin-down channels below the Fermi level, with no corresponding states above it (inset Fig. 4d). This fully occupied state signifies the complete reduction of O_2 to O_2^{2-}.

The adsorption of $^{\bullet}O_2^-$ notably alters the surface's conduction properties, as seen by the reduced E_g compared to the clean defective surface (Fig. SM5b‡). This effect can be attributed to the reduction of O_2, which forms a V_O^+ state. As previously reported,[31] the V_O^+ state in SnO_2 is unstable and quickly collapses, leading to its delocalization into the CB. This process is accompanied by a downward shift in the unoccupied energy levels.

2.4 Sensor mechanism

In agreement with previous findings,[41] our study confirmed that the dissociation of the O_2 molecule on the pristine, *i.e.*, fully oxidized, SnO_2 surface is highly unfavorable. In all cases considered, the dissociative reaction was always endergonic and demanded a high energy input.

The most promising dissociative reaction pathway starts with the physisorbed triplet oxygen on the SnO_2 (110) surface (Fig. SM-8‡) and culminates in the formation of two adsorbed O^- anions after the homolytic dissociation. However, this process demands a significant high energy input of 2.40 eV and results in an unstable product that is 2.34 eV higher in energy. Additionally, the reverse reaction barrier of 0.06 eV is negligible, therefore O_2 dissociation is not feasible following this pathway on the fully oxidized surface at ambient conditions.

Previously, we demonstrated that the coadsorption of molecules on a metal oxide semiconductor surface—specifically those that induce opposite and complementary charge transfer processes between the substrate and adsorbate (*e.g.*, a reducing agent alongside an oxidizing agent)—can result in a synergistic activation of both molecules.[55] Given that the sensor activity of CO on SnO_2 hinges on the interaction between an oxidizing molecule (O_2) and a reducing species (CO) to generate CO_2, we hypothesized that a similar synergistic effect could be replicated in our system and the coupling of O_2 dissociation with CO_2 formation would diminish the energy barriers involved.

With the $^3O_2$ molecule pre-adsorbed on the surface (intermediate 2 in Fig. 5a), the CO coadsorption is more favorable when both molecules have parallel bond axes. In this configuration, the oxygen atoms of each species are physisorbed onto adjacent Sn^{4+} cations within neighboring [SnO_{5c}] clusters (intermediate 3). The coadsorption shifts the initial adsorption energy to higher values, increasing from −0.23 to −0.10 eV,

primarily due to steric hindrance and electron repulsion between the oxygen atoms of the fully oxidized surface and CO. Despite this shift, coadsorption remains energetically favorable.

The crucial step of this reaction pathway involves the simultaneous cleavage of O_2's double bond with the formation of a carbon–oxygen bond between one oxygen atom and CO (TS1), resulting in physisorbed CO_2 and an adsorbed O^- anion (intermediate 4). The forbidding 2.40 eV of energy previously required for the homolytic dissociation of $^3O_2$ alone is significantly offset by its coupling with CO oxidation, reducing the energy input to 0.67 eV. This results in a product configuration that is 1.86 eV more stable. Since O_2 dissociation is kinetically controlled, it is expected that this reaction will be facilitated at temperatures above ambient, lowering the activation barrier to a more accessible energy range.

These findings reveal a critical shift in understanding the Mars–van Krevelen mechanism. Whereas O_2 dissociation and CO oxidation were previously thought to occur sequentially—with lattice oxygen being provided only after O_2 dissociation—our results show that these steps should instead be considered simultaneous. This not only enhances reaction efficiency but also results in a more stable product, in contrast to the unstable products observed when O_2 dissociation was considered in isolation.

The resultant CO_2 molecule is weakly physisorbed to the surface *via* van der Waals interactions, requiring only 0.15 eV for its desorption, a process that proceeds without a significant energy barrier or transition state since no chemical bonds are formed or broken. Once CO_2 desorbs (intermediate 5), the remaining O^- anion remains bound to a surface Sn cation, offering a favorable site for a subsequent CO molecule to adsorb (intermediate 6).

This newly adsorbed CO molecule is oxidised by the O^- anion with a mild energy input of 0.06 eV (TS2). The oxidation results in the formation of another weakly physisorbed CO_2 molecule, in a highly exergonic reaction that lowers the system's energy by 4.97 eV (intermediate 7). As with the first CO_2, its desorption involves the low energy of 0.09 eV, completing the catalytic cycle of CO oxidation on the pristine SnO_2 (110) surface.

Nevertheless, the energy required to trigger the sensor mechanism *via* the proposed reaction pathway should still be prohibitively high for practical applications. However, our previous analysis into the effects of V_O on the surface's functional activity has shown that the presence of these vacancies significantly alters the O_2 adsorption process, shifting its character from physisorption, dominated by weak dipole interactions, to chemisorption, where reactive oxygen species form due to charge transfer from the surface to the adsorbate. This charge transfer is facilitated by the availability of trapped electrons in the electron polaron shallow states formed by the vacancy. This spontaneous prior activation of O_2 upon adsorption is expected to facilitate the subsequent dissociation process, benefiting the entire CO oxidation mechanism.

We then selected the pathway for CO_2 formation beginning with the adsorption of O_2 onto the V_O site leading to the generation of the $^*O_2^-$ precursor. Initiating the mechanism with the more stable peroxide anion would require the prior breaking of the stable bond it forms with the surface Sn cation in the [SnO_5] cluster in addition to the molecular bond itself. This additional step would likely introduce an extra energy barrier or, at the very least, complicate the oxidative mechanism without altering the final products of the reaction. In contrast, the superoxide state circumvents this issue since one of its

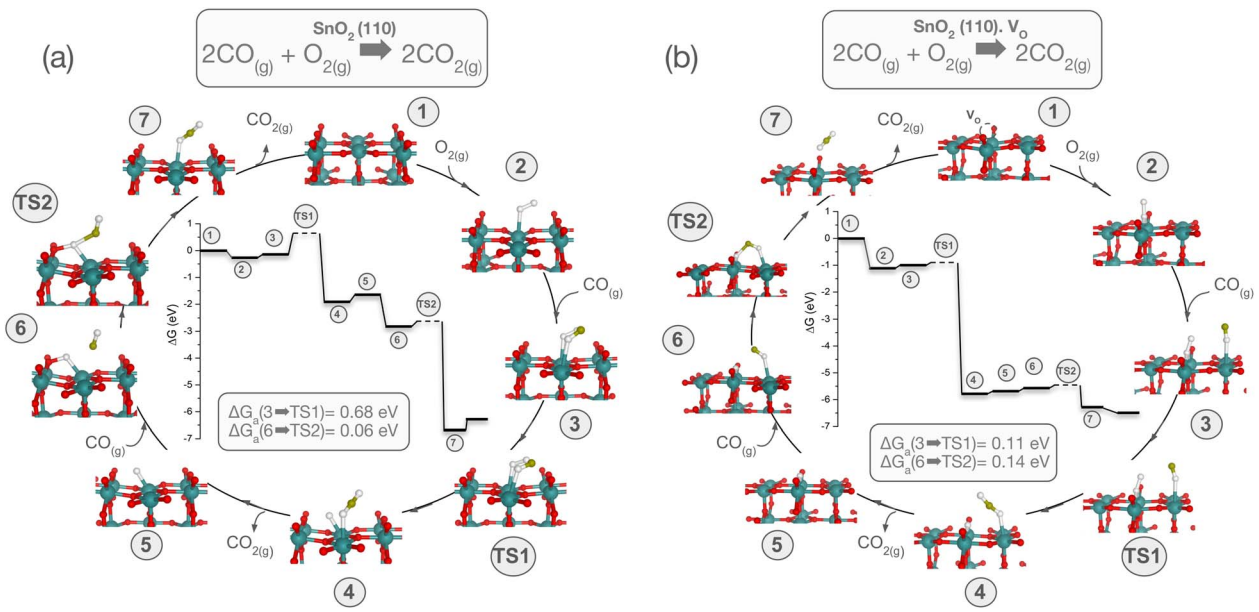

Fig. 5 Energy profiles and catalytic cycles along with the optimized structures of intermediates and transition states for CO oxidation catalyzed by the SnO_2 (110) (a) and SnO_2 (110)·V_O surfaces (b). Gibbs free activation energies (ΔG_a) for the relevant reaction steps are highlighted. The white and olive spheres represent O in O_2, CO, and CO_2, and C in CO and CO_2, respectively.

oxygen atoms remains unbound to the surface, and thus readily available to coordinate the CO molecule. By instead starting with the superoxide pathway, we avoid these complications and directly focus on the relevant processes, making this approach more suitable for assessing the emergence of any potential synergistic effects. We anticipate that, as observed in the previous catalytic cycle, this process occurs simultaneously with the weakening and breaking of the O_2 double bond, effectively offsetting the energy required for its dissociation. This reaction mechanism is illustrated in Fig. 5b.

The initial adsorption of O_2 at the V_O site generates the precursor of $^{\bullet}O_2^-$ *via* electron transfer from the surface's polaron A_1 state to the molecule's partially filled HOMO $2\pi^*$ (intermediate 2 in Fig. 5b). $^{\bullet}O_2^-$ and surface now establish a strong electrostatic interaction, which is reflected by the high adsorption free energy ($\Delta_{ad}G$) of −1.10 eV. The subsequent physisorption of a CO molecule, akin to its behavior observed previously on an V_O-free surface, is slightly unfavorable, reducing the total $\Delta_{ad}G$ to −1.05 eV. In this configuration, both molecular axes are roughly parallel to each other: O_2 adsorbed vertically on the vacancy site and the CO physisorbed through its oxygen atom to the adjacent cation of the [SnO_5] site (intermediate 3). Even the slightest tilt of the CO axis towards the O_2 triggers the immediate oxidative reaction, hinting at an energetically favorable process. Indeed, the transition state is formed by a virtually negligible energy input of 0.11 eV (TS1). The reaction culminates in the formation of CO_2 by the concomitant rupture of the O_2 double bond and binding with the CO. Distinctively from the vacancy-free scenario, now an O^{2-} anion remains bound to the surface along with a physisorbed CO_2, through a highly exergonic process with Δ_rG of −4.71 eV (intermediate 4). The O ion occupies the V_O site and is reduced by its electron polaron to O^{2-}.

This finding aligns with the study by Sopiha *et al.*,[41] which reported that O^{2-} ions are found to be exclusively stable on SnO_2 surfaces of n-type character, whose availability of electrons from the CB is crucial to stabilize the O^{2-}. Furthermore, this species was linked to the enhanced sensitivity of SnO_2-based sensors. In summary, the CO adsorption is enhanced by the presence of an electron polaron, where the charge carrier is attracted to the surface, and the carrier lifetime increases.

The physisorbed CO_2 is weakly bound *via* van der Waals interactions, requiring just 0.11 eV for complete desorption, a process that occurs without any bond dissociation (intermediate 5). Subsequent physisorption of a CO molecule at the Sn_{5c} site, adjacent to the adsorbed O^{2-}, proceeds in a similar fashion to the pristine surface, necessitating an energy input of 0.11 eV to overcome steric and electronic hindrances (intermediate 6). The oxidation reaction that follows decreases the total energy by 0.63 eV, surmounting a modest barrier of 0.14 eV (TS2). The resulting CO_2 remains weakly physisorbed (intermediate 7), and its desorption further lowers the system energy by 0.31 eV, fully restoring the catalytic surface, including the electron polaron. This restoration of the polaron plays a critical role in stabilizing the system and ensuring the surface remains catalytically active for subsequent reactions. This step completes the catalytic cycle of CO oxidation on the SnO_2 (110)·V_O surface.

This pathway is not only energetically favorable but also represents a paradigm shift in how we understand the Mars–van Krevelen mechanism. The previously accepted sequential steps of O_2 dissociation and CO oxidation are superseded by a more efficient process where both events occur simultaneously, leading to a reduction in activation barriers and a stabilization of intermediate species. Crucially, this shift is strongly supported by the coupling with the electron polaron, which enhances charge transfer and stabilizes reactive oxygen species such as $^{\bullet}O_2^-$ and O^{2-}. This spontaneous activation by the polaron facilitates the entire catalytic cycle, reinforcing the role of polarons as pivotal in optimizing sensor activity and catalytic performance on the SnO_2 surface. This mechanism—combining two independent processes, the polaron's role in enhancing O_2 activation and the synergistic interaction between O_2 dissociation and CO oxidation facilitated by the co-adsorption configuration—defines a novel and energetically favorable pathway for CO oxidation, paving the way for advanced applications.

3 Conclusions

Understanding the behavior of adsorbed O_2 on the SnO_2 surface is critical to unveiling the reaction mechanisms underpinning gas sensing. Our work reveals a critical advancement in understanding the gas-sensing mechanisms on the SnO_2 (110) surface, driven by the synergistic interplay between V_O and electron polarons. Through detailed DFT simulations, we demonstrate that polaron formation at V_O sites spontaneously activates O_2, directly coupling its dissociation with CO oxidation. This finding marks a critical shift in the Mars–van Krevelen mechanism, where O_2 dissociation and CO_2 formation are no longer treated as sequential steps but rather as simultaneous processes. This synergy drastically reduces energy barriers while stabilizing key reactive intermediates, making the overall reaction pathway more efficient.

Our findings underscore the polaron's pivotal role in driving the entire catalytic cycle, where its charge-stabilizing effect boosts the formation of reactive oxygen species such as $^{\bullet}O_2^-$ and O^{2-}. This polaron-mediated activation facilitates the CO oxidation pathway, resulting in an energetically optimized process that enhances sensor reactivity and performance. These insights highlight the importance of defect engineering and polaron formation in designing more efficient SnO_2-based sensors for real-world applications. Our main conclusions are as follows:

(i) We identified the Mars–van Krevelen mechanism as the most thermodynamically favorable pathway, where the dissociation of chemisorbed O_2 and the simultaneous formation of CO_2 are driven by V_O.

(ii) The spatial and electronic structure of the SnO_2 (110) surface, particularly V_O and the formation of electron polarons, significantly influence charge mobility and reactivity, thus facilitating efficient CO oxidation.

(iii) New states in the band gap and the shift in Fermi energy, induced by polaron formation and O_2 adsorption, favor the formation of $^{\bullet}O_2^-$, O^-, and O_2^{2-} species, critical to the gas-sensing mechanism.

(iv) A strong correlation is established between sensor activity and defect state energy levels, providing deeper insights into the redox processes involving O_2 and CO.

(v) DFT calculations reveal that sensor performance is governed by the intricate balance of adsorption intermediate stability, electron transfer process, and intermolecular interactions between the SnO_2 (110) surface an oxygen species adsorbed at this surface.

Future experimental validation of these findings will further clarify their practical implications. In particular, the current model of interaction between SnO_2 and oxygen species offers valuable insight into the mechanisms that prevent sintering in this semiconductor. Specifically, the decomposition of SnO_2 at elevated temperatures (300–800 °C), governed by the reaction $2\ SnO_2 \rightarrow 2\ SnO + O_2$, promotes the formation of oxygen vacancies (V_O), which in turn suppresses sintering. This work provides foundational knowledge for improving gas sensor designs through strategic defect manipulation, with potential applications extending across various metal oxide semiconductor technologies.

4 Computational methods

4.1 Structural relaxation

We performed a series of first-principles calculations based on density functional theory (DFT) as implemented in the Vienna *Ab initio* Simulation Package (VASP).[56,57] The generalized gradient approximation (GGA) by Perdew–Burke–Ernzerhof revised for solids (PBEsol)[57] was used to model the exchange–correlation functional, and the projector augmented wave (PAW) method[58,59] was employed to account for the core electrons. Dispersion interactions were included through Grimme's D3 method with Becke–Johnson damping.[60] All calculations were spin-polarized, a crucial step in accurately describing molecular adsorption and activation.

A plane-wave cut-off energy of 500 eV was applied to expand the valence electrons: Sn ($4d^{10}5s^25p^2$), O ($2s^22p^4$), and C ($2s^22p^2$). The Gaussian smearing method with a smearing width of 0.01 eV was used for the occupancy of one-electron states, and the total energies of all static calculations were corrected using the tetrahedron method[61] for Brillouin zone integrations.

Total energy and geometry optimization calculations were performed using automatically generated Monkhorst–Pack Γ-centered *k*-point grids[62] with dimensions of $7 \times 7 \times 10$ for bulk models and $5 \times 3 \times 1$ for surface models. The convergence criterion for geometry optimization was set to 10^{-8} eV for energy and 0.1×10^{-4} eV Å^{-1} for forces in bulk models, and 10^{-6} eV for energy and 0.1×10^{-1} eV Å^{-1} for surface models. Isolated CO and O_2 gas molecules were modeled in a $20 \times 30 \times 25$ Å^3 simulation box, with the same convergence criteria used for bulk SnO_2, and the Γ point was used to integrate the Brillouin zone.

4.2 Electronic calculations

In addition to the PBEsol functional, we employed the HSE06 hybrid screened functional[63] for the calculation of density of states (DOS), Mulliken charges, and band structure. It was found that the PBEsol functional provided an inadequate electronic description of the localized states arising from the formation of V_O in the SnO_2 surface. This functional's inability to fully cancel the electron self-interaction resulted in artificial delocalization of the wavefunction, leading to the localized single-particle state merging with the conduction band. This effect mirrors previously reported findings for similar systems,[64] which prompted us to adopt the same workaround.

The HSE06 functional, by offering partial cancellation of the self-interaction error, was therefore employed for the geometric optimization of the defective surface. This calculation utilized a plane-wave cutoff energy of 400 eV, and Brillouin zone integrations were performed using the Γ-point (0, 0, 0) and a high-symmetry *k*-point (1/4, 1/4, 0). This approach allowed for the correct description of the localized single-particle state created by the V_O.

4.3 Reaction pathways and transition states

Transition states for the elementary steps of the reactions were located using either the climbing-image nudged elastic band (CI-NEB) method[65] or the improved dimer method.[66] The force convergence criterion was set to 0.5×10^{-1} eV Å^{-1}, and all transition states were verified as true saddle points by confirming a single imaginary frequency mode along the reaction coordinate. The vibrational frequencies were calculated using a finite difference approach with a 0.015 Å displacement for each degree of freedom. For NEB calculations, nine intermediate images were initially generated using the image dependent pair potential method.[67] In cases where CI-NEB failed to converge to the exact saddle point according to vibrational calculations, the dimer method was employed to refine the transition state structures on the potential energy surface.

4.4 Calculation of Gibbs free energies

The relative Gibbs free energy values (ΔG) reported in this work, whether for reaction energy ($\Delta_r G$), activation energy ($\Delta_a G$), or adsorption energy ($\Delta_{ad} G$), were evaluated using the following expression:

$$G = E_{DFT} + ZPE + \int_0^T C_P\, dT - T\Delta S \quad (2)$$

The necessary values for zero-point energy (ZPE), entropy (ΔS), and heat capacity (C_P) were derived from the normal vibrational modes of the surface or adsorbed systems and gas-phase molecules, assuming a temperature of 298.15 K and a pressure of 101.3 kPa when not explicitly stated. Therefore, the energy values obtained by DFT calculations at 0 K with electronic smearing extrapolated to zero (E_{DFT}) were corrected accordingly.[68] These corrections were applied using the post-processing tool VASPKIT,[69] and only the vibrational modes from the ions of the first trilayer of the slab and the adsorbed molecules were considered.

4.5 Adsorption configurations

The adsorption energies ($\Delta_{ad} G$) were used to assess the stability of the adsorption configurations and are defined as:

$$\Delta_{ad} G = G_{adsorb/surf} - G_{surf} - G_{adsorb} \quad (3)$$

where $G_{adsorb/surf}$, G_{surf}, and G_{adsorb} represent the DFT total energies, corrected by eqn (2), for the slab with adsorbate(s), the clean slab, and the isolated adsorbate(s), respectively.

An extensive screening for potential adsorption configurations of one O_2 molecule on the pristine SnO_2 (110) surface was conducted using XSORB (version 2.0), a Python-based code that integrates *ab initio* calculations and two well-established Python libraries (ASE and Pymatgen) to generate the structures.[70] The program automatically samples the potential energy surface (PES) describing the molecule–surface interaction by generating several adsorption configurations through symmetry operations. The set of most stable configurations is identified *via* a fast pre-optimization scheme, and the PES global minimum is determined through a full structural optimization process. The generated symmetry-distinct adsorption sites (Fig. SM6‡), the energy values from both the pre- and full-optimization schemes (Table SM3‡), as well as the input data for the code, are available in the ESI.‡

Data availability

The data supporting this article have been included as part of the ESI.‡

Conflicts of interest

There are no conflicts to declare.

Acknowledgements

F. L. acknowledges the support from Coordenação de Aperfeiçoamento de Pessoal de Nível Superior (CAPES) for the CAPES-PRINT grant, process number 88887.695471/2022-00, and from Ministerio de Ciencia e Innovación for the postdoctoral grant from project PID2022-141089NB-I00. M. S.-M. acknowledges support from the São Paulo Research Foundation (FAPESP) for grants 2013/07296-2, 2016/23891-6, 2017/26105-4, and 2020/03780-0, CAPES, and the National Council for Scientific and Technological Development (CNPq) for grant 305792/2020-2. A. F. G. acknowledges the Generalitat Valenciana (Conselleria de Innovación, Universidades, Ciencia y Sociedad Digital) for the postdoctoral contract (grant #CIAPOS/2021/106). J. A. and M. O. acknowledge support from Ministerio de Ciencia e Innovación (project PID2022-141089NB-I00), Conselleria de Innovación, Universidades, Ciencia y Sociedad Digital (project CIAICO/2021/122) and Universitat Jaume I (project UJI-B2022-56). This work utilized computational resources provided by the Centro de Computação John David Rogers (CCJDR-UNICAMP) and by the Servei d'Informàtica (SI) of Universitat Jaume I.

References

1 Y. Kong, Y. Li, X. Cui, L. Su, D. Ma, T. Lai, L. Yao, X. Xiao and Y. Wang, *Nano Mater. Sci.*, 2022, **4**, 339–350.
2 M. Periyasamy and A. Kar, *J. Mater. Chem. C*, 2020, **8**, 4604–4635.
3 K. Suematsu, Y. Hiroyama, W. Harano, W. Mizukami, K. Watanabe and K. Shimanoe, *ACS Sens.*, 2020, **5**, 3449–3456.
4 X. Liu, X. Zhang, H. Tao, J. Huang, J. Huang, Y. Chen, W. Yuan, R. Yao, H. Ning and J. Peng, *Acta Phys. Sin.*, 2020, **69**, 228102.
5 S. Maeng, S.-W. Kim, D.-H. Lee, S.-E. Moon, K.-C. Kim and A. Maiti, *ACS Appl. Mater. Interfaces*, 2014, **6**, 357–363.
6 E. Kanazawa, M. Kugishima, K. Shimanoe, Y. Kanmura, Y. Teraoka, N. Miura and N. Yamazoe, *Sens. Actuators, B*, 2001, **75**, 121–124.
7 W. Yan, W. Ai, W. Liu, Z. Zhao, X. Hu, S. Cui and X. Shen, *J. Alloys Compd.*, 2023, **943**, 169042.
8 W. Zeng, T. Liu, Z. Wang, S. Tsukimoto, M. Saito and Y. Ikuhara, *Sensors*, 2009, **9**, 9029–9038.
9 M. Nitta, S. Ohtani and M. Haradome, *J. Electron. Mater.*, 1980, **9**, 727–743.
10 A. F. Gouveia, C. M. Aldao, M. A. Ponce, E. R. Leite, E. Longo and J. Andrés, *Appl. Surf. Sci.*, 2023, **622**, 156904.
11 Q. Liu, H. Zhan, X. Huang, Y. Song, S. He, X. Li, C. Wang and Z. Xie, *Eur. J. Inorg. Chem.*, 2021, **2021**, 4370–4376.
12 J. A. Varela, L. A. Perazolli, E. Longo, E. R. Leite and J. A. Cerri, *Radiat. Eff. Defects Solids*, 1998, **146**, 131–143.
13 D. Mirabella, P. Desimone, M. Ponce, C. Aldao, L. da Silva, A. Catto and E. Longo, *Sens. Actuators, B*, 2021, **329**, 129253.
14 L. Hao, H. Huang, Y. Zhang and T. Ma, *Adv. Funct. Mater.*, 2021, **31**, 2100919.
15 Q. Hou, J. Buckeridge, T. Lazauskas, D. Mora-Fonz, A. A. Sokol, S. M. Woodley and C. R. A. Catlow, *J. Mater. Chem. C*, 2018, **6**, 12386–12395.
16 J. Wang, J. Chang, S. Kang, Y. Chen and S. Fan, *Mater. Today Commun.*, 2023, **37**, 107632.
17 C. Franchini, M. Reticcioli, M. Setvin and U. Diebold, *Nat. Rev. Mater.*, 2021, **6**, 560–586.
18 P. Gono, J. Wiktor, F. Ambrosio and A. Pasquarello, *ACS Catal.*, 2018, **8**, 5847–5851.
19 Q. Zeng, Y. Cui, L. Zhu and Y. Yao, *Mater. Sci. Semicond. Process.*, 2020, **111**, 104962.
20 M. Al-Hashem, S. Akbar and P. Morris, *Sens. Actuators, B*, 2019, **301**, 126845.
21 I. Sokolović, M. Reticcioli, M. Čalkovský, M. Wagner, M. Schmid, C. Franchini, U. Diebold and M. Setvín, *Proc. Natl. Acad. Sci. U. S. A.*, 2020, **117**, 14827–14837.
22 Y. Yoon, Y.-G. Wang, R. Rousseau and V.-A. Glezakou, *ACS Catal.*, 2015, **5**, 1764–1771.
23 A. Dey, *Mater. Sci. Eng., B*, 2018, **229**, 206–217.
24 H. Ji, W. Zeng and Y. Li, *Nanoscale*, 2019, **11**, 22664–22684.
25 A. Mirzaei, S. Leonardi and G. Neri, *Ceram. Int.*, 2016, **42**, 15119–15141.
26 P. Desimone, F. Schipani, R. Procaccini, D. Mirabella and C. Aldao, *Sens. Actuators, B*, 2022, **370**, 132387.
27 D. Degler, U. Weimar and N. Barsan, *ACS Sens.*, 2019, **4**, 2228–2249.
28 A. Gurlo, *ChemPhysChem*, 2006, **7**, 2041–2052.
29 K. Hauffe, *Angew. Chem.*, 1955, **67**, 189–207.
30 Y.-F. Sun, S.-B. Liu, F.-L. Meng, J.-Y. Liu, Z. Jin, L.-T. Kong and J.-H. Liu, *Sensors*, 2012, **12**, 2610–2631.

31 L. Zhao, X. Gong, W. Tao, T. Wang, P. Sun, F. Liu, X. Liang, F. Liu, Y. Wang and G. Lu, *ACS Sens.*, 2022, **7**, 1095–1104.
32 D. A. Mirabella and C. M. Aldao, *ACS Sens.*, 2023, **8**, 397–399.
33 L. Zhao, X. Gong, W. Tao, T. Wang, P. Sun, F. Liu, X. Liang, F. Liu and G. Lu, *ACS Sens.*, 2023, **8**, 400–402.
34 Q. Fu and T. Wagner, *Surf. Sci. Rep.*, 2007, **62**, 431–498.
35 X. Li, W. Feng, Y. Xiao, P. Sun, X. Hu, K. Shimanoe, G. Lu and N. Yamazoe, *RSC Adv.*, 2014, **4**, 28005–28010.
36 S. Kucharski and C. Blackman, *Chemosensors*, 2021, **9**, 270.
37 N. Goel, K. Kunal, A. Kushwaha and M. Kumar, *Eng. Rep.*, 2023, **5**, e12604.
38 D. A. Mirabella and C. M. Aldao, *ACS Sens.*, 2024, **9**, 1938–1944.
39 N. Barsan and U. Weimar, *J. Electroceram.*, 2001, **7**, 143–167.
40 N. Yamazoe, G. Sakai and K. Shimanoe, *Catal. Surv. Asia*, 2003, **7**, 63–75.
41 K. V. Sopiha, O. I. Malyi, C. Persson and P. Wu, *ACS Appl. Mater. Interfaces*, 2021, **13**, 33664–33676.
42 S. You, G. Li, Z. Fan, X. Li, L. Fu and W. Wu, *Int. J. Electrochem. Sci.*, 2023, **18**, 100314.
43 Y. He and M. Jiao, *Chemosensors*, 2024, **12**, 55.
44 T. Nandy, R. A. Coutu and C. Ababei, *Sensors*, 2018, **18**, 3443.
45 Y. Zhang, J. Liu, C. Rong, D. Wang, W. Li, Z. Gao and Y. Chen, *Langmuir*, 2024, **40**, 18821–18836.
46 A. A. Firooz, A. R. Mahjoub and A. A. Khodadadi, *Sens. Actuators, B*, 2009, **141**, 89–96.
47 N. Bârsan, M. Hübner and U. Weimar, *Sens. Actuators, B*, 2011, **157**, 510–517.
48 Y. Chen, H. Qin and J. Hu, *Appl. Surf. Sci.*, 2018, **428**, 207–217.
49 Z. Lu, D. Ma, L. Yang, X. Wang, G. Xu and Z. Yang, *Phys. Chem. Chem. Phys.*, 2014, **16**, 12488–12494.
50 P. Ágoston and K. Albe, *Surf. Sci.*, 2011, **605**, 714–722.
51 T. Yamanaka, R. Kurashima and J. Mimaki, *Z. Kristallogr.–Cryst. Mater.*, 2000, **215**, 424–428.
52 M. Karmaoui, A. B. Jorge, P. F. McMillan, A. E. Aliev, R. C. Pullar, J. A. Labrincha and D. M. Tobaldi, *ACS Omega*, 2018, **3**, 13227–13238.
53 J. Oviedo and M. Gillan, *Surf. Sci.*, 2000, **463**, 93–101.
54 C. Freysoldt, B. Grabowski, T. Hickel, J. Neugebauer, G. Kresse, A. Janotti and C. G. Van de Walle, *Rev. Mod. Phys.*, 2014, **86**, 253–305.
55 F. Lipsky, L. H. d. S. Lacerda, L. Gracia, B. G. Foschiani, M. Assis, M. Oliva, E. Longo, J. Andrés and M. A. San-Miguel, *J. Phys. Chem. C*, 2023, **127**, 23235–23245.
56 G. Kresse and J. Furthmüller, *Comput. Mater. Sci.*, 1996, **6**, 15–50.
57 G. Kresse and J. Furthmüller, *Phys. Rev. B:Condens. Matter Mater. Phys.*, 1996, **54**, 11169–11186.
58 G. Kresse and D. Joubert, *Phys. Rev. B:Condens. Matter Mater. Phys.*, 1999, **59**, 1758–1775.
59 P. E. Blöchl, *Phys. Rev. B:Condens. Matter Mater. Phys.*, 1994, **50**, 17953–17979.
60 S. Grimme, S. Ehrlich and L. Goerigk, *J. Comput. Chem.*, 2011, **32**, 1456–1465.
61 P. E. Blöchl, O. Jepsen and O. K. Andersen, *Phys. Rev. B:Condens. Matter Mater. Phys.*, 1994, **49**, 16223–16233.
62 H. J. Monkhorst and J. D. Pack, *Phys. Rev. B*, 1976, **13**, 5188–5192.
63 A. V. Krukau, O. A. Vydrov, A. F. Izmaylov and G. E. Scuseria, *J. Chem. Phys.*, 2006, **125**, 224106.
64 A. Janotti, J. B. Varley, P. Rinke, N. Umezawa, G. Kresse and C. G. Van de Walle, *Phys. Rev. B:Condens. Matter Mater. Phys.*, 2010, **81**, 085212.
65 G. Henkelman, B. P. Uberuaga and H. Jónsson, *J. Chem. Phys.*, 2000, **113**, 9901–9904.
66 A. Heyden, A. T. Bell and F. J. Keil, *J. Chem. Phys.*, 2005, **123**, 224101.
67 S. Smidstrup, A. Pedersen, K. Stokbro and H. Jónsson, *J. Chem. Phys.*, 2014, **140**, 214106.
68 L. I. Bendavid and E. A. Carter, *J. Phys. Chem. C*, 2013, **117**, 26048–26059.
69 V. Wang, N. Xu, J.-C. Liu, G. Tang and W.-T. Geng, *Comput. Phys. Commun.*, 2021, **267**, 108033.
70 E. Pedretti, P. Restuccia and M. C. Righi, *Comput. Phys. Commun.*, 2023, **291**, 108827.